

Multiscale modeling of viscoelastic plant tissue

Pieter Ghysels

Giovanni Samaey

Paul Van Liedekerke

Engelbert Tjiskens

Herman Ramon

Dirk Roose

Report TW 550, November 2009



Katholieke Universiteit Leuven
Department of Computer Science

Celestijnenlaan 200A – B-3001 Heverlee (Belgium)

Multiscale modeling of viscoelastic plant tissue

Pieter Ghysels

Giovanni Samaey

Paul Van Liedekerke

Engelbert Tijskens

Herman Ramon

Dirk Roose

Report TW 550, November 2009

Department of Computer Science, K.U.Leuven

Abstract

We present a multiscale method for the simulation of large viscoelastic deformations and show its applicability to biological tissue such as plant tissue. At the microscopic level we use a particle method to model the geometrical structure and basic properties of individual cells. The cell fluid, modeled as a viscoelastic fluid by means of *Smoothed Particle Hydrodynamics (SPH)* is enclosed in an elastic cell wall, modeled by discrete elements. The macroscopic equation and stress tensor are derived from the SPH model by means of the *Generalized Mathematical Homogenization* technique. The macroscopic domain is discretized using standard finite elements, where the stress tensor is evaluated from microscopic simulations in small sub-domains, called *Representative Volume Elements (RVEs)*. Our emphasis is on reconstructing the microscopic state inside the RVE for given macroscopic deformation and velocity gradient. We propose a scheme to initialize the RVE consistently not only with the macroscopic variables, but also with the microscopic dynamics.

Keywords : RVE, computational homogenization, biological tissue deformation, micromechanics, SPH

MSC : Primary : 35B27, Secondary : 35Q70, 92C80.

Multiscale modeling of viscoelastic plant tissue

P. Ghysels*, G. Samaey*, P. Van Liedekerke†, E. Tijskens†, H. Ramon†, D. Roose*

November 3, 2009

Abstract

We present a multiscale method for the simulation of large viscoelastic deformations and show its applicability to biological tissue such as plant tissue. At the microscopic level we use a particle method to model the geometrical structure and basic properties of individual cells. The cell fluid, modeled as a viscoelastic fluid by means of *Smoothed Particle Hydrodynamics (SPH)* is enclosed in an elastic cell wall, modeled by discrete elements. The macroscopic equation and stress tensor are derived from the SPH model by means of the *Generalized Mathematical Homogenization* technique. The macroscopic domain is discretized using standard finite elements, where the stress tensor is evaluated from microscopic simulations in small sub-domains, called *Representative Volume Elements (RVEs)*. Our emphasis is on reconstructing the microscopic state inside the RVE for given macroscopic deformation and velocity gradient. We propose a scheme to initialize the RVE consistently not only with the macroscopic variables, but also with the microscopic dynamics.

Keywords: RVE, computational homogenization, biological tissue deformation, micromechanics, SPH

1 Introduction

Plant tissue is a material with a distinct multiscale nature, in which properties at the (microscopic) cellular level influence the (macroscopic) tissue behavior in a highly non-trivial way. Although one could propose a constitutive *model* of plant tissue at a macroscopic scale [17, 22, 3], such models do not *explain* how the underlying cell level properties affect the overall macroscopic behavior of the tissue. An alternative approach is to develop physical models which appreciate the cellular level, and to use this microscopic model for simulations at the tissue level.

A drawback of such microscopic simulations over large spatio-temporal scales is their associated computational cost. This paper is devoted to a computational multiscale strategy that exploits the relation between the microscopic (cellular) level and the macroscopic (tissue) level to significantly reduce the required simulation time with the microscopic model. The method is an extension of the micro-macro coupling strategy based on the concept of Representative Volume Elements (RVEs) [15, 7, 20], which was already extended to deal with the case of elastic deformations of plant tissue in [11]. The macroscopic continuum equation, in which the constitutive stress strain relation is not explicitly known, is discretized on the whole domain using standard finite elements, and integrated in time. In each quadrature point, we apply a given deformation on an RVE and perform an appropriate microscopic simulation. The required stresses are then evaluated on the fly using a stress expression corresponding to the mechanical part of the virial stress. The main goal of this paper is to show how these microscopic simulations need to be carried out to recover the viscoelastic deformation behavior at the tissue level. To this end, we derive a dynamical microscopic problem to be solved inside the RVEs, together with a corresponding macroscopic

*K.U.Leuven - Department of Computer Science, Celestijnenlaan 200A - bus 2402, B-3001 Heverlee - Belgium, Tel.: +32-16-327700, pieter.ghysels@cs.kuleuven.be

†K.U.Leuven - Department of Biosystems, Kasteelpark Arenberg 30 - bus 2456, B-3001 Heverlee - Belgium

continuum equation. This derivation is based on the framework of generalized mathematical homogenization (GMH) [5, 4, 8].

The microscopic model that will be used, developed by Van Liedekerke *et al* [27, 26], explicitly incorporates the cell fluid and cell wall viscosity. Therefore, it is able to model the dynamic and static behavior of plant cells and aggregates with arbitrary cell shapes, possibly subjected to large deformations. Both the solid phase (cell wall) and the fluid inside the cell (cytoplasm) are considered. The viscoelastic cell fluid is modeled using Smoothed Particle Hydrodynamics (SPH) [23, 24] and the cell wall by the Discrete Element Method (DEM) [6].

The main contributions of this paper are twofold. First, we extend the GMH technique to deal with the velocity dependency of the inter-particle forces, i.e. the viscosity of the material. This leads to a dynamic problem to be solved inside the RVE, in which not only a deformation gradient has to be applied to the RVE, but also a velocity gradient. Second, a computational method is proposed to initialize the RVE consistently with the macroscopic variables and at the same time consistent with the microscopic dynamics. The method is based on the constrained runs approach [9, 10], originally proposed as a part of the equation-free framework [13, 14]. We remark that a simple relaxation to the elastic equilibrium is not possible since this would alter the macroscopic observables, i.e. the velocity and/or the deformation. The scheme we propose to reconstruct the microscopic state inside the RVE for given macroscopic deformation and velocity gradients is an iteration of two steps: a short time integration followed by a rescaling of the RVE. The time integration allows an internal relaxation of the RVE while the rescaling ensures that the overall deformation and velocity gradients of the RVE (the macroscopic observables) correspond to the given macroscopic gradients.

The paper is organized as follows. In section 2, we discuss the computational microscopic (cellular) model, including a brief description of both the SPH and DEM methods for the cell fluid, resp. cell wall. The coupled particle system can be written under the general form of Newton's second law of motion. Section 3 then performs a two-scale expansion. We derive a microscopic and a macroscopic equation as well as the necessary coupling relations using an extension of GMH to visco-elastic deformation. Section 5 focuses on solving the problem inside the RVE for given macroscopic observables and introduces the constrained runs iteration to consistently initialize the RVE, i.e. reconstructing the microscopic state inside the RVE for given macroscopic deformation and velocity gradient. Section 6 numerically illustrates the accuracy of the proposed approach and shows its importance by comparing to simpler initialization schemes. We conclude the paper and give an outlook in section 7.

2 Microscopic (cellular) model

In this paper, we use a Lagrangian mesh-free particle method for parenchyma plant cell tissue, similar to the method introduced in [27]. The model considers both the solid phase, the cell wall, and the more fluid-like phase, the cytoplasm. We first describe the mechanical model for the cell wall, based on the DEM, followed by a discussion on the SPH method for the cell fluid. The reader is referred to [27] for more details. Note that the microscopic scale here corresponds to the cellular scale of plant tissue, and could therefore also be denoted as the mesoscopic scale.

2.1 Solid cell wall

The solid cell wall is considered as a thin viscoelastic solid which offers no resistance to bending. The wall is coarse grained by particles as in the *discrete element method (DEM)* [6]. Neighboring particles on the cell wall are bonded by a linear elastic spring and a dashpot while a strong repulsive force prevents non-neighboring particles from overlapping. Let \mathbf{x}_i , \mathbf{v}_i and m_i denote the position, velocity and mass of a particle i . The relative distance and velocity of two particles are denoted by $\mathbf{x}_{ij} = \mathbf{x}_j - \mathbf{x}_i$ and $\mathbf{v}_{ij} = \mathbf{v}_j - \mathbf{v}_i$ respectively. The force on a cell wall particle i from

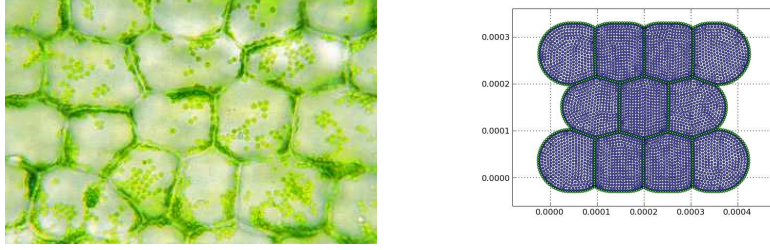


Figure 1: Taken from [27]. Left: cell structure of real plants. Right: an in silico sample of plant parenchyma tissue. The green discrete elements model the viscoelastic cell wall, shared between adjacent cells, the blue dots represent the SPH particles.

its neighboring particles l and non-neighboring particles k is given by

$$\mathbf{F}_i = - \sum_l (k_w (|\mathbf{x}_{ik}| - l_0) + \gamma_c \mathbf{x}_{il} \cdot \mathbf{v}_{il}) \frac{\mathbf{x}_{il}}{|\mathbf{x}_{il}|} + \sum_k f_{ik} \frac{\mathbf{x}_{ik}}{|\mathbf{x}_{ik}|} \quad (1)$$

where k_w is the strength of the harmonic contact, l_0 the initial length of the contact and $\gamma_c = 2\sqrt{m_i k_w}$ a viscous damping parameter, chosen to get critical damping. The repulsive force f_{ik} is defined as

$$f_{ik} = \lambda \left(\frac{1}{|\mathbf{x}_{ik}|^6} - \frac{1}{x_0^6} \right) - 2\sqrt{\frac{6\lambda m_i}{|\mathbf{x}_{ik}|^7}} \mathbf{x}_{ik} \cdot \mathbf{v}_{ik} \quad \text{for } |\mathbf{x}_{ik}| \leq x_0, \quad 0 \quad \text{otherwise} \quad (2)$$

with λ the strength and x_0 a cutoff distance. The second, velocity dependent term in (2) critically damps the repulsive force. This critical damping was introduced for numerical stability. In the model, two neighboring cells share one cell wall, making it impossible for two cells to slip along each other or to debond. The masses of the particles in such a combined cell wall are computed from the mass of the combination of the two cell walls and the middle lamella in between. The internals of the plant cell are modeled as a viscous fluid using SPH, see 2.2. The SPH-DEM fluid-structure interaction is based on the repulsive force (2), where the summation over non-neighboring particles k in (1) also includes the SPH particles. The opposite force $-f_{ik}\mathbf{x}_{ik}/|\mathbf{x}_{ik}|$ is applied to the SPH particles.

2.2 Viscous cell fluid

We now turn to the cell fluid, which is modeled via SPH. The exposition on SPH below closely follows [24].

In the smoothed particle hydrodynamics technique, the equations of motion of a set of (meso-scale) particles are integrated in time. Associated with each particle is a kernel function. Macroscopic variables of interest, such as pressure, density, velocity, are obtained by interpolation of the particle values by means of their kernel functions. The SPH approximation for a function $f(\mathbf{x})$ would thus be

$$\langle f(\mathbf{x}) \rangle = \sum_j^N f(\mathbf{x}_j) W(\mathbf{x} - \mathbf{x}_j, h) dV_j \approx f(\mathbf{x}), \quad (3)$$

with dV_j a volume element associated to particle j , and $W(\mathbf{x} - \mathbf{x}_j, h)$ the kernel function with smoothing length h . Ideally this kernel function closely approximates a Gaussian. Furthermore, it has to satisfy

$$\lim_{h \rightarrow 0} W(\mathbf{x}, h) = \delta(\mathbf{x}), \quad \text{and} \quad \int_{-\infty}^{\infty} W(\mathbf{x}, h) d\mathbf{x} = 1, \quad (4)$$

and it has to be symmetric. A popular choice for the kernel function is a cubic spline since it has compact support and its second order derivatives are continuous. It is given by

$$W(\mathbf{x}, h) = \frac{\sigma}{h^\nu} \begin{cases} (1 - \frac{3}{2}s^2 + \frac{3}{4}s^3), & 0 \leq s \leq 1, \\ \frac{1}{4}(2-s)^3, & 1 \leq s \leq 2, \\ 0, & \text{otherwise,} \end{cases} \quad (5)$$

where $s = \|\mathbf{x}\|/h$, ν the number of spatial dimensions, and σ a scaling parameter.

Let m_j and $\rho(\mathbf{x}_j)$ denote the mass and density of particle j respectively. Then, after defining $dV_j = m_j/\rho(\mathbf{x}_j)$, the SPH approximation to the density field can be written as

$$\langle \rho(\mathbf{x}) \rangle = \sum_{j=1}^N m_j W(\mathbf{x} - \mathbf{x}_j, h). \quad (6)$$

We will denote the density of particle i at position \mathbf{x}_i by

$$\rho_i = \rho(\mathbf{x}_i) = \sum_{j=1}^N m_j W_{ij} \quad (7)$$

with $W(\mathbf{x}_i - \mathbf{x}_j, h) = W(\mathbf{x}_{ji}, h) = W_{ji} = W_{ij}$. To model a viscous fluid using SPH, we use the momentum equation

$$\frac{d\mathbf{v}_i}{dt} = - \sum_j m_j \left(\frac{p_i}{\rho_i^2} + \frac{p_j}{\rho_j^2} \right) \left(\frac{\mathbf{x}_{ij}}{\|\mathbf{x}_{ij}\|} \frac{\partial W_{ij}}{\partial x_i} \right) + \sum_j \frac{m_j (\mu_i + \mu_j) \mathbf{v}_{ij}}{\rho_i \rho_j} \left(\frac{1}{\|\mathbf{x}_{ij}\|} \frac{\partial W_{ij}}{\partial x_i} \right) \quad (8)$$

with p_i , resp. μ_i , are the pressure, resp. dynamic viscosity, at \mathbf{x}_i . The pressure is computed using the equation of state

$$p = c_s^2 \rho \quad (9)$$

where c_s is the speed of sound. Several alternatives to this equation of state are described in the literature, see for instance [16].

Remark 1. A popular alternative way to compute the density at a given point is based on the continuity equation $d\rho/dt = -\rho \nabla \cdot \mathbf{v}$. This leads to an ordinary differential equation for the densities which has to be integrated simultaneously with (8). Here we use the summation density approach (7) instead of the continuity based approach since it is more accurate in the conservation of mass and because it allows us to write the complete SPH method in the general form given in equation (10), see section 3.

Remark 2. Because the kernel function has compact support, particles further than $r > 2h$ do not interact. For accuracy of the interpolations, there should always be approximately the same number of particles inside the zone of influence of each particle. To achieve this, the smoothing length can be adjusted. This will not be considered further since introducing the smoothing length as an extra variable per particle would complicate the derivations in section 3.

3 Generalized mathematical homogenization

We now derive a macroscopic continuum equation from the microscopic particle model using generalized mathematical homogenization [5, 4, 8]. The equation of motion (8) for a particle and for a point mass in the discrete element method can, omitting all external forces, be written as

$$m_i \frac{d\mathbf{v}_i}{dt} = \sum_j \mathbf{f}_{ij}(\mathbf{x}_{ij}, \mathbf{v}_{ij}), \quad (10)$$

where \mathbf{x}_{ij} and \mathbf{v}_{ij} denote $\mathbf{x}_j - \mathbf{x}_i$ and $\mathbf{v}_j - \mathbf{v}_i$, respectively. We introduce a discrete displacement field as follows: If \mathbf{x}_i denotes the current position of an SPH particle and \mathbf{X}_i denotes the original position, i.e. the position at time $t = 0$, then

$$\mathbf{x}_i = \mathbf{X}_i + \mathbf{u}_i, \quad (11)$$

with \mathbf{u}_i the displacement of particle i . The displacement field can be written as a function of the original coordinates \mathbf{X}_i , i.e. $\mathbf{u}(\mathbf{X}_i, t)$ (the material description), or as a function of the current, deformed coordinates, i.e. $\mathbf{u}(\mathbf{x}_i, t)$ (the spatial description).

We now proceed to derive a macroscopic description starting from these equations. The exposition closely follows [8]; we have, however, extended the derivation to also include viscous deformation, which will appear to be important for plant tissue. This viscous term is a direct consequence of the fact that the inter-particle forces depend directly on the particle velocities; the analysis will reveal that, on the macroscopic scale, this results in a dependence of the stress tensor on the velocity gradient.

3.1 Multiple spatio-temporal scales and rescaled microscopic equations

We introduce two distinct material coordinates to describe the continuum scale and the microscopic scale. Let \mathbf{X} coordinates denote the macroscopic scale, at which microscopic features are invisible, and let the microscopic features be captured by the coordinates \mathbf{Y} . The two scales are related by

$$\mathbf{Y} = \frac{\mathbf{X}}{\epsilon} \quad 0 < \epsilon \ll 1. \quad (12)$$

The corresponding spatial coordinates are given as \mathbf{x} and $\mathbf{y} = \mathbf{x}/\epsilon$. In the same way, we introduce a fast time variable τ , related to the standard time t by

$$\tau = \frac{t}{\epsilon} \quad 0 < \epsilon \ll 1. \quad (13)$$

With these notations, the first two material time derivatives of the displacement field are obtained using the chain rule as

$$\dot{\mathbf{u}}_i(\mathbf{X}_i, \mathbf{Y}_i, t, \tau) = \dot{\mathbf{u}}(\mathbf{X}, \mathbf{Y}_i, t, \tau) = \frac{d\mathbf{u}(\mathbf{X}, \mathbf{Y}_i, t, \tau)}{dt} = \frac{\partial \mathbf{u}}{\partial t} + \epsilon^{-1} \frac{\partial \mathbf{u}}{\partial \tau} \quad (14)$$

$$\ddot{\mathbf{u}}_i(\mathbf{X}_i, \mathbf{Y}_i, t, \tau) = \left(\frac{\partial}{\partial t} + \epsilon^{-1} \frac{\partial}{\partial \tau} \right) \left(\frac{\partial \mathbf{u}}{\partial t} + \epsilon^{-1} \frac{\partial \mathbf{u}}{\partial \tau} \right). \quad (15)$$

To carry out a multiscale asymptotic analysis, we also need to rescale the microscopic equations. Consider the (macroscopic) continuum equation $\rho \dot{\mathbf{v}}(\mathbf{x}, t) = \nabla_{\mathbf{x}} \cdot \boldsymbol{\sigma}$, with $\boldsymbol{\sigma}$ the Cauchy stress tensor, $\nabla_{\mathbf{x}} \cdot$ the divergence operator, ρ the material density and $\dot{\mathbf{v}}$ the acceleration. In a homogeneous material, the stress derivatives are $\nabla_{\mathbf{x}} \cdot \boldsymbol{\sigma} \sim \mathcal{O}(1)$, while in a heterogeneous medium they can be $\nabla_{\mathbf{x}} \cdot \boldsymbol{\sigma} \sim \mathcal{O}(\epsilon^{-1})$. Let us assume $\rho \sim \mathcal{O}(1)$ and the characteristic length of the RVE is $l \sim \mathcal{O}(\epsilon)$. The volume of a two-dimensional RVE is $V_{\text{RVE}} \sim \mathcal{O}(\epsilon^2)$ and from this the mass $m_i \sim \rho V_{\text{RVE}} \sim \mathcal{O}(\epsilon^2)$. Dividing equation (10) by the RVE volume yields

$$k_1 \rho \frac{d\mathbf{v}_i(\mathbf{X}_i, \mathbf{Y}_i, t, \tau)}{dt} = \frac{1}{k_2 \epsilon^2} \sum_j \mathbf{f}_{ij}(\mathbf{x}_{ij}, \mathbf{v}_{ij}) \quad (16)$$

with $k_1, k_2 \sim \mathcal{O}(1)$. The right-hand-side of (16) can be identified with the stress divergence term from the continuum equation, which is $\mathcal{O}(\epsilon^{-1})$. Defining the rescaled variables

$$\bar{\mathbf{f}}_{ij}(\mathbf{x}_{ij}, \mathbf{v}_{ij}) = \frac{\mathbf{f}_{ij}(\mathbf{x}_{ij}, \mathbf{v}_{ij})}{\epsilon} \sim \mathcal{O}(1), \quad \bar{m}_i = \frac{m_i}{\epsilon^2} \sim \mathcal{O}(1), \quad (17)$$

leads to the rescaled SPH equation of motion

$$\bar{m}_i \frac{d\mathbf{v}_i(\mathbf{X}_i, \mathbf{Y}_i, t, \tau)}{dt} = \frac{1}{\epsilon} \sum_j \bar{\mathbf{f}}_{ij}(\mathbf{x}_{ij}, \mathbf{v}_{ij}). \quad (18)$$

3.2 Multiscale asymptotic analysis

Suppose the macro scale \mathbf{X} is a continuum while the micro coordinates \mathbf{Y}_i are discrete. The displacement of particle i at macro point $\mathbf{X} = \mathbf{X}_i$ is given by $\mathbf{u}(\mathbf{X}, \mathbf{Y}_i, t, \tau)$. The displacements of neighboring particles $\mathbf{u}_j(\mathbf{X}_j, \mathbf{Y}_j, t, \tau)$ can be expanded using Taylor series around the point \mathbf{X}

$$\mathbf{u}_j = \mathbf{u}(\mathbf{X}_j, \mathbf{Y}_j, t, \tau) \quad (19)$$

$$\begin{aligned} &= \mathbf{u}(\mathbf{X}, \mathbf{Y}_j, t, \tau) + \nabla_{\mathbf{X}} \mathbf{u}(\mathbf{X}, \mathbf{Y}_j, t, \tau) \cdot (\mathbf{X}_j - \mathbf{X}_i) \\ &\quad + \frac{1}{2} \nabla_{\mathbf{X}}^2 \mathbf{u}(\mathbf{X}, \mathbf{Y}_j, t, \tau) : ((\mathbf{X}_j - \mathbf{X}_i) \otimes (\mathbf{X}_j - \mathbf{X}_i)) + \dots, \end{aligned} \quad (20)$$

and since $\mathbf{X}_j - \mathbf{X}_i = \epsilon(\mathbf{Y}_j - \mathbf{Y}_i) = \epsilon \mathbf{Y}_{ij}$, we have

$$\mathbf{u}_j - \mathbf{u}_i = \mathbf{u}(\mathbf{X}_j, \mathbf{Y}_j, t, \tau) - \mathbf{u}(\mathbf{X}_i, \mathbf{Y}_i, t, \tau) \quad (21)$$

$$\begin{aligned} &= \mathbf{u}(\mathbf{X}, \mathbf{Y}_j, t, \tau) - \mathbf{u}(\mathbf{X}, \mathbf{Y}_i, t, \tau) + \epsilon \nabla_{\mathbf{X}} \mathbf{u}(\mathbf{X}, \mathbf{Y}_j, t, \tau) \cdot \mathbf{Y}_{ij} \\ &\quad + \frac{\epsilon^2}{2} \nabla_{\mathbf{X}}^2 \mathbf{u}(\mathbf{X}, \mathbf{Y}_j, t, \tau) : (\mathbf{Y}_{ij} \otimes \mathbf{Y}_{ij}) + \dots \end{aligned} \quad (22)$$

The assumption of separation in spatial scales leads to a multiple scale asymptotic expansion for the displacement field of the form

$$\mathbf{u}(\mathbf{X}, \mathbf{Y}, t, \tau) = \mathbf{u}^0(\mathbf{X}, t) + \epsilon \mathbf{u}^1(\mathbf{X}, \mathbf{Y}, t, \tau) + \dots \quad (23)$$

where the term \mathbf{u}^0 represents the macroscopic displacement, independent of the fine scale coordinates \mathbf{Y} and the fast time scale τ . Since we consider a periodic microstructure, the fine scale perturbations $\mathbf{u}^1(\mathbf{X}, \mathbf{Y}, t, \tau)$ are periodic in \mathbf{Y} . Furthermore, we will also assume \mathbf{u}^1 to be periodic in τ . With expansion (23), (22) can be written as

$$\begin{aligned} \mathbf{u}_j - \mathbf{u}_i &= \epsilon \left(\mathbf{u}^1(\mathbf{X}, \mathbf{Y}_j, t, \tau) - \mathbf{u}^1(\mathbf{X}, \mathbf{Y}_i, t, \tau) + \nabla_{\mathbf{X}} \mathbf{u}^0(\mathbf{X}, t) \cdot \mathbf{Y}_{ij} \right) + \\ &\quad \epsilon^2 \left(\nabla_{\mathbf{X}} \mathbf{u}^1(\mathbf{X}, \mathbf{Y}_j, t, \tau) \cdot \mathbf{Y}_{ij} + \frac{1}{2} \nabla_{\mathbf{X}}^2 \mathbf{u}^0(\mathbf{X}, t) : (\mathbf{Y}_{ij} \otimes \mathbf{Y}_{ij}) \right) + \dots \end{aligned} \quad (24)$$

Recalling the standard definition of the macroscopic deformation gradient,

$$\mathbf{F}^0(\mathbf{X}, t) = \mathbf{I} + \nabla_{\mathbf{X}} \mathbf{u}^0(\mathbf{X}, t), \quad (25)$$

this leads to an expansion for $\mathbf{x}_j - \mathbf{x}_i$

$$\mathbf{x}_{ij} = \mathbf{x}_j - \mathbf{x}_i = \mathbf{X}_{ij} + \mathbf{u}_j - \mathbf{u}_i = \epsilon \phi_{ij}(\mathbf{X}, \mathbf{Y}, t, \tau) + \epsilon^2 \psi_{ij}(\mathbf{X}, \mathbf{Y}, t, \tau) + \dots \quad (26)$$

with

$$\begin{aligned} \phi_{ij}(\mathbf{X}, \mathbf{Y}, t, \tau) &= \mathbf{Y}_{ij} + \mathbf{u}^1(\mathbf{X}, \mathbf{Y}_j, t, \tau) - \mathbf{u}^1(\mathbf{X}, \mathbf{Y}_i, t, \tau) + \nabla_{\mathbf{X}} \mathbf{u}^0(\mathbf{X}, t) \cdot \mathbf{Y}_{ij} \\ &= \mathbf{F}^0(\mathbf{X}, t) \cdot \mathbf{Y}_{ij} + \mathbf{u}^1(\mathbf{X}, \mathbf{Y}_j, t, \tau) - \mathbf{u}^1(\mathbf{X}, \mathbf{Y}_i, t, \tau) \end{aligned} \quad (27)$$

$$\psi_{ij}(\mathbf{X}, \mathbf{Y}, t, \tau) = \nabla_{\mathbf{X}} \mathbf{u}^1(\mathbf{X}, \mathbf{Y}_j, t, \tau) \cdot \mathbf{Y}_{ij} + \frac{1}{2} \nabla_{\mathbf{X}}^2 \mathbf{u}^0(\mathbf{X}, t) : (\mathbf{Y}_{ij} \otimes \mathbf{Y}_{ij}). \quad (28)$$

Likewise, for the velocities, the multiple scale asymptotic expansion is written as

$$\mathbf{v}_{ij} = \mathbf{v}_j - \mathbf{v}_i = \frac{d\mathbf{x}_{ij}}{dt} = \epsilon \xi_{ij}(\mathbf{X}, \mathbf{Y}, t, \tau) + \epsilon^2 \theta_{ij}(\mathbf{X}, \mathbf{Y}, t, \tau) + \dots \quad (29)$$

where ξ_{ij} and θ_{ij} are the time derivatives of ϕ_{ij} and ψ_{ij} respectively,

$$\xi_{ij}(\mathbf{X}, \mathbf{Y}, t, \tau) = \frac{d\phi_{ij}}{dt} = \dot{\mathbf{F}}^0(\mathbf{X}, t) \cdot \mathbf{Y}_{ij} + \mathbf{v}^1(\mathbf{X}, \mathbf{Y}_j, t, \tau) - \mathbf{v}^1(\mathbf{X}, \mathbf{Y}_i, t, \tau) \quad (30)$$

$$\theta_{ij}(\mathbf{X}, \mathbf{Y}, t, \tau) = \frac{d\psi_{ij}}{dt} = \nabla_{\mathbf{X}} \mathbf{v}^1(\mathbf{X}, \mathbf{Y}_j, t, \tau) \cdot \mathbf{Y}_{ij} + \frac{1}{2} \nabla_{\mathbf{X}}^2 \mathbf{v}^0(\mathbf{X}, t) : (\mathbf{Y}_{ij} \otimes \mathbf{Y}_{ij}), \quad (31)$$

with $\mathbf{v} = \dot{\mathbf{u}} = d\mathbf{u}/dt$ and $d\mathbf{Y}_{ij}/dt = 0$. Since

$$\frac{\|\epsilon^2 \boldsymbol{\psi}_{ij}(\mathbf{X}, \mathbf{Y}, t, \tau)\|}{\|\epsilon \boldsymbol{\phi}_{ij}(\mathbf{X}, \mathbf{Y}, t, \tau)\|} \sim \mathcal{O}(\epsilon) \quad \text{and} \quad \frac{\|\epsilon^2 \boldsymbol{\theta}_{ij}(\mathbf{X}, \mathbf{Y}, t, \tau)\|}{\|\epsilon \boldsymbol{\xi}_{ij}(\mathbf{X}, \mathbf{Y}, t, \tau)\|} \sim \mathcal{O}(\epsilon) \quad (32)$$

the inter-particle force can be Taylor expanded around $(\epsilon \boldsymbol{\phi}_{ij}, \epsilon \boldsymbol{\xi}_{ij})$ as

$$\begin{aligned} \bar{\mathbf{f}}_{ij}(\mathbf{x}_{ij}, \mathbf{v}_{ij}) &\approx \bar{\mathbf{f}}_{ij}(\epsilon \boldsymbol{\phi}_{ij} + \epsilon^2 \boldsymbol{\psi}_{ij}, \epsilon \boldsymbol{\xi}_{ij} + \epsilon^2 \boldsymbol{\theta}_{ij}) \\ &= \bar{\mathbf{f}}_{ij}(\epsilon \boldsymbol{\phi}_{ij}, \epsilon \boldsymbol{\xi}_{ij}) + \frac{\partial \bar{\mathbf{f}}_{ij}}{\partial \mathbf{x}_{ij}}(\epsilon \boldsymbol{\phi}_{ij}, \epsilon \boldsymbol{\xi}_{ij}) \cdot \epsilon^2 \boldsymbol{\psi}_{ij} + \frac{\partial \bar{\mathbf{f}}_{ij}}{\partial \mathbf{v}_{ij}}(\epsilon \boldsymbol{\phi}_{ij}, \epsilon \boldsymbol{\xi}_{ij}) \cdot \epsilon^2 \boldsymbol{\theta}_{ij} + \mathcal{O}(\epsilon^2). \end{aligned} \quad (33)$$

The multiple scale expansion for the acceleration field is found by taking the second material time derivative (15) of the multiple scale expansion for the displacement,

$$\ddot{\mathbf{u}}_i(\mathbf{X}_i, \mathbf{Y}_i, t, \tau) = \epsilon^{-1} \frac{\partial^2 \mathbf{u}^1}{\partial \tau^2} + \frac{\partial^2 \mathbf{u}^0}{\partial t^2} + 2 \frac{\partial^2 \mathbf{u}^1}{\partial t \partial \tau} + \epsilon \frac{\partial^2 \mathbf{u}^1}{\partial t^2} + \mathcal{O}(\epsilon^2). \quad (34)$$

The rescaled equation of motion (18) is expanded using (34) and (33) to

$$\begin{aligned} \bar{m}_i \left(\epsilon^{-1} \frac{\partial^2 \mathbf{u}^1}{\partial \tau^2} + \frac{\partial^2 \mathbf{u}^0}{\partial t^2} + 2 \frac{\partial^2 \mathbf{u}^1}{\partial t \partial \tau} + \epsilon \frac{\partial^2 \mathbf{u}^1}{\partial t^2} + \mathcal{O}(\epsilon^2) \right) = \\ \frac{1}{\epsilon} \sum_j \left[\bar{\mathbf{f}}_{ij}(\epsilon \boldsymbol{\phi}_{ij}, \epsilon \boldsymbol{\xi}_{ij}) + \frac{\partial \bar{\mathbf{f}}_{ij}}{\partial \mathbf{x}_{ij}}(\epsilon \boldsymbol{\phi}_{ij}, \epsilon \boldsymbol{\xi}_{ij}) \cdot \epsilon^2 \boldsymbol{\psi}_{ij} + \frac{\partial \bar{\mathbf{f}}_{ij}}{\partial \mathbf{v}_{ij}}(\epsilon \boldsymbol{\phi}_{ij}, \epsilon \boldsymbol{\xi}_{ij}) \cdot \epsilon^2 \boldsymbol{\theta}_{ij} + \mathcal{O}(\epsilon^2) \right]. \end{aligned} \quad (35)$$

Collecting terms with equal powers of ϵ leads to an equation with $\mathcal{O}(\epsilon^{-1})$ terms,

$$\bar{m}_i \frac{\partial^2 \mathbf{u}^1(\mathbf{X}, \mathbf{Y}_i, t, \tau)}{\partial \tau^2} = \sum_j \bar{\mathbf{f}}_{ij}(\epsilon \boldsymbol{\phi}_{ij}, \epsilon \boldsymbol{\xi}_{ij}), \quad (36)$$

which defines the micro-scale problem, and to an equation with $\mathcal{O}(1)$ terms,

$$\bar{m}_i \left(\frac{\partial^2 \mathbf{u}^0(\mathbf{X}, t)}{\partial t^2} + 2 \frac{\partial^2 \mathbf{u}^1(\mathbf{X}, \mathbf{Y}_i, t, \tau)}{\partial t \partial \tau} \right) = \sum_j \left[\frac{\partial \bar{\mathbf{f}}_{ij}}{\partial \mathbf{x}_{ij}}(\epsilon \boldsymbol{\phi}_{ij}, \epsilon \boldsymbol{\xi}_{ij}) \cdot \epsilon \boldsymbol{\psi}_{ij} + \frac{\partial \bar{\mathbf{f}}_{ij}}{\partial \mathbf{v}_{ij}}(\epsilon \boldsymbol{\phi}_{ij}, \epsilon \boldsymbol{\xi}_{ij}) \cdot \epsilon \boldsymbol{\theta}_{ij} \right], \quad (37)$$

i.e. the macroscopic problem. Note that for a heterogeneous material, the inter-particle force derivatives are $\mathcal{O}(\epsilon^{-1})$. In the next two subsections, these micro and macro equations are investigated further.

3.3 The micro problem

From the definitions for $\boldsymbol{\phi}_{ij}$ (27) and $\boldsymbol{\xi}_{ij}$ (30), together with $\epsilon \mathbf{Y}_{ij} = \mathbf{X}_{ij}$ we have

$$\begin{aligned} \epsilon \boldsymbol{\phi}_{ij}(\mathbf{X}, \mathbf{Y}, t, \tau) &= \epsilon (\mathbf{F}^0(\mathbf{X}, t) \cdot \mathbf{Y}_{ij} + \mathbf{u}^1(\mathbf{X}, \mathbf{Y}_j, t, \tau) - \mathbf{u}^1(\mathbf{X}, \mathbf{Y}_i, t, \tau)) \\ &= \mathbf{F}^0(\mathbf{X}, t) \cdot \mathbf{X}_{ij} + \epsilon \mathbf{u}^1(\mathbf{X}, \mathbf{Y}_j, t, \tau) - \epsilon \mathbf{u}^1(\mathbf{X}, \mathbf{Y}_i, t, \tau) \end{aligned} \quad (38)$$

$$\epsilon \boldsymbol{\xi}_{ij}(\mathbf{X}, \mathbf{Y}, t, \tau) = \dot{\mathbf{F}}^0(\mathbf{X}, t) \cdot \mathbf{X}_{ij} + \epsilon \mathbf{v}^1(\mathbf{X}, \mathbf{Y}_j, t, \tau) - \epsilon \mathbf{v}^1(\mathbf{X}, \mathbf{Y}_i, t, \tau), \quad (39)$$

and the microscopic equation (36) can thus be rewritten as

$$\boxed{\bar{m}_i \frac{\partial^2 \mathbf{u}^1(\mathbf{X}, \mathbf{Y}_i, t, \tau)}{\partial \tau^2} = \sum_j \bar{\mathbf{f}}_{ij} \left(\mathbf{F}^0(\mathbf{X}, t) \cdot \mathbf{X}_{ij} + \epsilon (\mathbf{u}_j^1 - \mathbf{u}_i^1), \dot{\mathbf{F}}^0(\mathbf{X}, t) \cdot \mathbf{X}_{ij} + \epsilon (\mathbf{v}_j^1 - \mathbf{v}_i^1) \right) \quad \forall i} \quad (40)$$

Assuming the microstructure is periodic in \mathbf{Y} , we can restrict the solution of this micro problem to a unit cell for each value of \mathbf{X} . Section 5 will focus on solving this problem numerically; the unit cell will correspond to the representative volume element (RVE).

3.4 The macro equation

The coarse scale equation (37) can be written, using the original unscaled mass and inter-particle forces, as

$$m_i \left(\frac{\partial^2 \mathbf{u}^0(\mathbf{X}, t)}{\partial t^2} + 2 \frac{\partial^2 \mathbf{u}^1(\mathbf{X}, \mathbf{Y}_i, t, \tau)}{\partial t \partial \tau} \right) = \epsilon \sum_j \left[\frac{\partial \mathbf{f}_{ij}}{\partial \mathbf{x}_{ij}}(\epsilon \phi_{ij}, \epsilon \boldsymbol{\xi}_{ij}) \cdot \epsilon \boldsymbol{\psi}_{ij} + \frac{\partial \mathbf{f}_{ij}}{\partial \mathbf{v}_{ij}}(\epsilon \phi_{ij}, \epsilon \boldsymbol{\xi}_{ij}) \cdot \epsilon \boldsymbol{\theta}_{ij} \right]. \quad (41)$$

Summation over all particles in the RVE and dividing by the initial volume of the RVE yields

$$\frac{1}{V_{\text{RVE}}^0} \sum_i \left[m_i \left(\frac{\partial^2 \mathbf{u}^0(\mathbf{x}, t)}{\partial t^2} + 2 \frac{\partial^2 \mathbf{u}^1(\mathbf{X}, \mathbf{Y}_i, t, \tau)}{\partial t \partial \tau} \right) \right] = \frac{\epsilon}{V_{\text{RVE}}^0} \sum_i \sum_j \left[\frac{\partial \mathbf{f}_{ij}}{\partial \mathbf{x}_{ij}}(\epsilon \phi_{ij}, \epsilon \boldsymbol{\xi}_{ij}) \cdot \epsilon \boldsymbol{\psi}_{ij} + \frac{\partial \mathbf{f}_{ij}}{\partial \mathbf{v}_{ij}}(\epsilon \phi_{ij}, \epsilon \boldsymbol{\xi}_{ij}) \cdot \epsilon \boldsymbol{\theta}_{ij} \right]. \quad (42)$$

The inner summation over all particles interacting with particle i can also be interpreted as a summation over the particles in the RVE, since an interacting particle outside the RVE corresponds to another particle inside the RVE by periodicity. Let $\langle \cdot \rangle$ define the temporal averaging operator over a time interval τ_0

$$\langle \cdot \rangle = \frac{1}{\tau_0} \int_0^{\tau_0} \cdot \, d\tau, \quad (43)$$

then

$$\left\langle \frac{1}{V_{\text{RVE}}^0} \sum_i \left[m_i \frac{\partial^2 \mathbf{u}^0(\mathbf{X}, t)}{\partial t^2} \right] \right\rangle = \frac{\epsilon}{V_{\text{RVE}}^0} \left\langle \sum_i \sum_j \left[\frac{\partial \mathbf{f}_{ij}}{\partial \mathbf{x}_{ij}}(\epsilon \phi_{ij}, \epsilon \boldsymbol{\xi}_{ij}) \cdot \epsilon \boldsymbol{\psi}_{ij} + \frac{\partial \mathbf{f}_{ij}}{\partial \mathbf{v}_{ij}}(\epsilon \phi_{ij}, \epsilon \boldsymbol{\xi}_{ij}) \cdot \epsilon \boldsymbol{\theta}_{ij} \right] \right\rangle, \quad (44)$$

where the second term in the left-hand-side of (41) vanished due to periodicity of \mathbf{u}^1 in τ . And since the left hand side is independent of τ

$$\rho_0 \frac{\partial^2 \mathbf{u}^0(\mathbf{X}, t)}{\partial t^2} = \frac{\epsilon}{V_{\text{RVE}}^0} \left\langle \sum_i \sum_j \left[\frac{\partial \mathbf{f}_{ij}}{\partial \mathbf{x}_{ij}}(\epsilon \phi_{ij}, \epsilon \boldsymbol{\xi}_{ij}) \cdot \epsilon \boldsymbol{\psi}_{ij} + \frac{\partial \mathbf{f}_{ij}}{\partial \mathbf{v}_{ij}}(\epsilon \phi_{ij}, \epsilon \boldsymbol{\xi}_{ij}) \cdot \epsilon \boldsymbol{\theta}_{ij} \right] \right\rangle. \quad (45)$$

By the chain rule we have

$$\begin{aligned} \nabla_{\mathbf{X}} \mathbf{f}_{ij}(\epsilon \phi_{ij}, \epsilon \boldsymbol{\xi}_{ij}) &= \frac{d\mathbf{f}_{ij}}{d\mathbf{X}}(\epsilon \phi_{ij}, \epsilon \boldsymbol{\xi}_{ij}) \\ &= \left(\frac{\partial \mathbf{f}_{ij}}{\partial \mathbf{x}_{ij}} \cdot \frac{\partial \mathbf{x}_{ij}}{\partial \mathbf{X}} \right) \Big|_{(\epsilon \phi_{ij}, \epsilon \boldsymbol{\xi}_{ij})} + \left(\frac{\partial \mathbf{f}_{ij}}{\partial \mathbf{v}_{ij}} \cdot \frac{\partial \mathbf{v}_{ij}}{\partial \mathbf{X}} \right) \Big|_{(\epsilon \phi_{ij}, \epsilon \boldsymbol{\xi}_{ij})} \\ &= \frac{\partial \mathbf{f}_{ij}}{\partial \mathbf{x}_{ij}}(\epsilon \phi_{ij}, \epsilon \boldsymbol{\xi}_{ij}) \cdot \frac{\partial \epsilon \phi_{ij}}{\partial \mathbf{X}} + \frac{\partial \mathbf{f}_{ij}}{\partial \mathbf{v}_{ij}}(\epsilon \phi_{ij}, \epsilon \boldsymbol{\xi}_{ij}) \cdot \frac{\partial \epsilon \boldsymbol{\xi}_{ij}}{\partial \mathbf{X}} \\ &= \frac{\partial \mathbf{f}_{ij}}{\partial \mathbf{x}_{ij}} \cdot \epsilon [\nabla_{\mathbf{X}}^2 \mathbf{u}^0(\mathbf{X}, t) \cdot \mathbf{Y}_{ij} + \nabla_{\mathbf{X}} \mathbf{u}^1(\mathbf{X}, \mathbf{Y}_j, t, \tau) - \nabla_{\mathbf{X}} \mathbf{u}^1(\mathbf{X}, \mathbf{Y}_i, t, \tau)] \\ &\quad + \frac{\partial \mathbf{f}_{ij}}{\partial \mathbf{v}_{ij}} \cdot \epsilon [\nabla_{\mathbf{X}}^2 \mathbf{v}^0(\mathbf{X}, t) \cdot \mathbf{Y}_{ij} + \nabla_{\mathbf{X}} \mathbf{v}^1(\mathbf{X}, \mathbf{Y}_j, t, \tau) - \nabla_{\mathbf{X}} \mathbf{v}^1(\mathbf{X}, \mathbf{Y}_i, t, \tau)]. \end{aligned} \quad (46)$$

From some simple algebra, it follows that

$$\begin{aligned} \epsilon \boldsymbol{\psi}_{ij}(\mathbf{X}, \mathbf{Y}, t, \tau) &= \frac{1}{2} (\nabla_{\mathbf{X}}^2 \mathbf{u}^0(\mathbf{X}, t) \cdot \mathbf{Y}_{ij} + \nabla_{\mathbf{X}} \mathbf{u}^1(\mathbf{X}, \mathbf{Y}_j, t, \tau) - \nabla_{\mathbf{X}} \mathbf{u}^1(\mathbf{X}, \mathbf{Y}_i, t, \tau)) \cdot \mathbf{X}_{ij} \\ &\quad + \frac{1}{2} (\nabla_{\mathbf{X}} \mathbf{u}^1(\mathbf{X}, \mathbf{Y}_i, t, \tau) + \nabla_{\mathbf{X}} \mathbf{u}^1(\mathbf{X}, \mathbf{Y}_j, t, \tau)) \cdot \mathbf{X}_{ij} \\ &= \frac{1}{2} \frac{\partial \phi_{ij}}{\partial \mathbf{X}} \cdot \mathbf{X}_{ij} + \frac{1}{2} (\nabla_{\mathbf{X}} \mathbf{u}^1(\mathbf{X}, \mathbf{Y}_i, t, \tau) + \nabla_{\mathbf{X}} \mathbf{u}^1(\mathbf{X}, \mathbf{Y}_j, t, \tau)) \cdot \mathbf{X}_{ij} \end{aligned} \quad (47)$$

and similarly

$$\epsilon \boldsymbol{\theta}_{ij}(\mathbf{X}, \mathbf{Y}, t, \tau) = \frac{1}{2} \frac{\partial \boldsymbol{\xi}_{ij}}{\partial \mathbf{X}} \cdot \mathbf{X}_{ij} + \frac{1}{2} (\nabla_{\mathbf{X}} \mathbf{v}^1(\mathbf{X}, \mathbf{Y}_i, t, \tau) + \nabla_{\mathbf{X}} \mathbf{v}^1(\mathbf{X}, \mathbf{Y}_j, t, \tau)) \cdot \mathbf{X}_{ij}. \quad (48)$$

Combining (47) and (48) with (46) transforms (45) into

$$\begin{aligned} \rho_0 \frac{\partial^2 \mathbf{u}^0(\mathbf{X}, t)}{\partial t^2} &= \frac{1}{2V_{\text{RVE}}^0} \left\langle \sum_i \sum_j \nabla_{\mathbf{X}} \mathbf{f}_{ij}(\epsilon \boldsymbol{\phi}_{ij}, \epsilon \boldsymbol{\xi}_{ij}) \cdot \mathbf{X}_{ij} \right\rangle \\ &\quad - \frac{1}{2V_{\text{RVE}}^0} \left\langle \sum_i \sum_j \left[\frac{1}{2} \left(\frac{\partial \mathbf{f}_{ij}}{\partial \mathbf{x}_{ij}} \cdot \nabla_{\mathbf{X}} [\mathbf{u}_i^1 + \mathbf{u}_j^1] + \frac{\partial \mathbf{f}_{ij}}{\partial \mathbf{v}_{ij}} \cdot \nabla_{\mathbf{X}} [\mathbf{v}_i^1 + \mathbf{v}_j^1] \right) \cdot \mathbf{X}_{ij} \right] \right\rangle. \end{aligned} \quad (49)$$

Using the well-known relation $\nabla_{\mathbf{X}} \cdot (\mathbf{v} \otimes \mathbf{w}) = \mathbf{v} \nabla_{\mathbf{X}} \cdot \mathbf{w} + \nabla_{\mathbf{X}} \mathbf{v} \cdot \mathbf{w}$ and since $\nabla_{\mathbf{X}} \cdot \mathbf{X}_{ij} = 0$, the coarse scale equation becomes

$$\begin{aligned} \rho_0 \frac{\partial^2 \mathbf{u}^0(\mathbf{X}, t)}{\partial t^2} &= \frac{1}{2V_{\text{RVE}}^0} \left\langle \sum_i \sum_j \nabla_{\mathbf{X}} \cdot (\mathbf{f}_{ij}(\epsilon \boldsymbol{\phi}_{ij}, \epsilon \boldsymbol{\xi}_{ij}) \otimes \mathbf{X}_{ij}) \right\rangle \\ &\quad - \frac{1}{2V_{\text{RVE}}^0} \left\langle \sum_i \sum_j \left[\frac{1}{2} \left(\frac{\partial \mathbf{f}_{ij}}{\partial \mathbf{x}_{ij}} \cdot \nabla_{\mathbf{X}} [\mathbf{u}_i^1 + \mathbf{u}_j^1] + \frac{\partial \mathbf{f}_{ij}}{\partial \mathbf{v}_{ij}} \cdot \nabla_{\mathbf{X}} [\mathbf{v}_i^1 + \mathbf{v}_j^1] \right) \cdot \mathbf{X}_{ij} \right] \right\rangle. \end{aligned} \quad (50)$$

From $\mathbf{x}_{ij} = -\mathbf{x}_{ji}$, $\epsilon \boldsymbol{\phi}_{ij} = \epsilon \boldsymbol{\phi}_{ji}$, $\epsilon \boldsymbol{\xi}_{ij} = \epsilon \boldsymbol{\xi}_{ji}$ and Newton's third law

$$\mathbf{f}_{ij}(\epsilon \boldsymbol{\phi}_{ij}, \epsilon \boldsymbol{\xi}_{ij}) = -\mathbf{f}_{ji}(\epsilon \boldsymbol{\phi}_{ji}, \epsilon \boldsymbol{\xi}_{ji}) \quad (51)$$

it follows that

$$\frac{\partial \mathbf{f}_{ij}}{\partial \mathbf{x}_{ij}}(\epsilon \boldsymbol{\phi}_{ij}, \epsilon \boldsymbol{\xi}_{ij}) \equiv \frac{\partial \mathbf{f}_{ji}}{\partial \mathbf{x}_{ji}}(\epsilon \boldsymbol{\phi}_{ji}, \epsilon \boldsymbol{\xi}_{ji}) \quad \text{and} \quad \frac{\partial \mathbf{f}_{ij}}{\partial \mathbf{v}_{ij}}(\epsilon \boldsymbol{\phi}_{ij}, \epsilon \boldsymbol{\xi}_{ij}) \equiv \frac{\partial \mathbf{f}_{ji}}{\partial \mathbf{v}_{ji}}(\epsilon \boldsymbol{\phi}_{ji}, \epsilon \boldsymbol{\xi}_{ji}). \quad (52)$$

Since also $\mathbf{X}_{ij} = -\mathbf{X}_{ji}$, the second double summation in the right-hand-side of (50) is zero since the ij term cancels with the ji term. We have recovered the classical continuum equation

$$\rho_0 \frac{\partial^2 \mathbf{u}^0(\mathbf{X}, t)}{\partial t^2} = \nabla_{\mathbf{X}} \cdot \langle \mathbf{P} \rangle \quad (53)$$

$$\mathbf{P}(\mathbf{X}, t, \tau) = \frac{1}{2V_{\text{RVE}}^0} \sum_i \sum_j \mathbf{f}_{ij}(\epsilon \boldsymbol{\phi}_{ij}, \epsilon \boldsymbol{\xi}_{ij}) \otimes \mathbf{X}_{ij} \quad (54)$$

with $\mathbf{P}(\mathbf{X}, t, \tau)$ the first Piola-Kirchhoff stress tensor. Dividing (54) by $J = \det \mathbf{F}(\mathbf{X}, \mathbf{Y}, t, \tau)$ and multiplying with $\mathbf{F}^T(\mathbf{X}, \mathbf{Y}, t, \tau)$ on the right leads to

$$J^{-1} \mathbf{P}(\mathbf{X}, t, \tau) \mathbf{F}^T(\mathbf{X}, \mathbf{Y}, t, \tau) = \frac{1}{2JV_{\text{RVE}}^0} \sum_i \sum_j \mathbf{f}_{ij}(\epsilon \boldsymbol{\phi}_{ij}, \epsilon \boldsymbol{\xi}_{ij}) \otimes \mathbf{X}_{ij} \cdot \mathbf{F}^T(\mathbf{X}, \mathbf{Y}, t, \tau) \quad (55)$$

$$\boldsymbol{\sigma}(\mathbf{x}, t, \tau) = \frac{1}{2V_{\text{RVE}}} \sum_i \sum_j \mathbf{f}_{ij}(\epsilon \boldsymbol{\phi}_{ij}, \epsilon \boldsymbol{\xi}_{ij}) \otimes \mathbf{x}_{ij} \quad (56)$$

where the well-known relation $\boldsymbol{\sigma} = J^{-1} \mathbf{P} \mathbf{F}^T$ between the Cauchy stress $\boldsymbol{\sigma}$ and the Piola-Kirchhoff stress \mathbf{P} was used. The coarse scale equation can now be written entirely in the spatial configuration as

$$\boxed{\begin{aligned} \rho \frac{\partial^2 \mathbf{u}^0(\mathbf{x}, t)}{\partial t^2} &= \nabla_{\mathbf{x}} \cdot \langle \boldsymbol{\sigma} \rangle \\ \boldsymbol{\sigma}(\mathbf{x}, t, \tau) &= \frac{1}{2V_{\text{RVE}}} \sum_i \sum_j \mathbf{f}_{ij}(\epsilon \boldsymbol{\phi}_{ij}, \epsilon \boldsymbol{\xi}_{ij}) \otimes \mathbf{x}_{ij} \end{aligned}} \quad (57)$$

Note that the definition of the stress tensor here corresponds to the mechanical part of the virial stress.

4 Finite element discretization

We now propose our computational multiscale approach, in which this macroscopic continuum equation is discretized using finite elements [2], and supplemented with a microscopic simulation in a representative volume element (RVE) around each quadrature point.

At the macroscopic level, we have chosen to use an updated Lagrangian formulation, but an equivalent total Lagrangian formulation is also conceivable [28], and would not influence the multiscale coupling strategy of the present paper. Rewriting the governing macro equation (57) in its weak form leads to a nonlinear equation for the displacement field. The domain κ_t is approximated by a set of n_{el} finite elements κ_e , in which the continuum displacement field $\mathbf{u} = \mathbf{x} - \mathbf{X}$ is approximated by $\mathbf{u} \approx \sum_a N_a \tilde{\mathbf{u}}_a$ where $\tilde{\mathbf{u}}_i$ are the displacements only defined in the discrete nodal positions and N_a is the shape function corresponding to node a . The discretization of the spatial macro equation (57) becomes

$$\mathbf{M} \frac{d^2 \tilde{\mathbf{u}}_i}{dt^2} = \sum_e^{n_{el}} \left(\int_{\kappa_e} \boldsymbol{\sigma} \nabla N_a dv - \int_{\kappa_e} \nabla N_a \mathbf{g} dv \right) \quad \forall i, \quad (58)$$

with \mathbf{g} the external body forces and \mathbf{M} the mass matrix, with elements

$$\mathbf{M}_{ab} = \sum_e^{n_{el}} \left(\int_{\kappa_e} N_a^T \rho N_b dv \right). \quad (59)$$

The second order system of ordinary differential equations (58) can be integrated using standard time-stepping algorithms [12].

In each quadrature point, the Cauchy stress is obtained using the stress formula (57b), applied to an appropriately initialized RVE. Such RVE-based methods are often used in materials science [7, 20, 15]; we refer to [11] for an application to the elastic deformation of plant tissue. The next section discusses the RVE initialization when viscous effects are important.

5 Initializing the micro problem

The problem to be solved inside the RVE, equation (40), receives displacements and velocities as input from the macroscopic model through $\mathbf{F}^0(\mathbf{X}, t)$ and $\dot{\mathbf{F}}^0(\mathbf{X}, t)$, which will determine the boundary conditions for the unit cell. Solving the microscopic equation means finding a state of the RVE that is consistent with these boundary conditions. However, since there are many more degrees of freedom inside the RVE, the solution is not unique. The solution one is generally interested in, is that particular configuration of the RVE that would occur if it was embedded in a larger domain of a full microscopic simulation. From this observation we conclude that the RVE should be consistent not only with the macroscopic input variables, but also with the microscopic system dynamics.

We will now first discuss how the macroscopic state is imposed on the RVE via appropriate boundary conditions, and then outline three increasingly accurate methods to reconstruct the microscopic state inside the RVE.

5.1 Boundary conditions

Let ∂V_{RVE} denote the entire RVE boundary and ∂V_{RVE}^D the Dirichlet part of the boundary. For Dirichlet boundary conditions, the position of each cell wall particle needs to be prescribed as $\mathbf{x}_i = \mathbf{F}^0(\mathbf{X}, t) \cdot \mathbf{X}_i$, $\forall i \in \partial V_{RVE}^D \equiv \partial V_{RVE}$. For periodic boundary conditions, only the displacements of three corners ($\partial V_{RVE}^D = [p_1 p_2 p_3]$) are prescribed as

$$[\mathbf{x}_1 \quad \mathbf{x}_2 \quad \mathbf{x}_3] = \mathbf{F}^0(\mathbf{X}, t) \cdot [\mathbf{X}_1 \quad \mathbf{X}_2 \quad \mathbf{X}_3] \quad (60)$$

together with periodicity constraints on the rest of the boundary, see [19, 11]. This is illustrated in figure 2. Corner p_1 will be assumed to be at the origin. Corner p_4 depends on the other corners

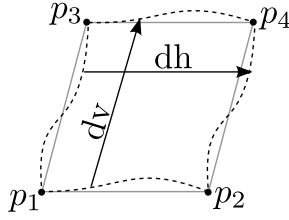


Figure 2: Illustration of a periodical RVE deformed with a shear deformation.

through the periodicity constraints. Both for the Dirichlet and the periodic boundary conditions, it can be shown that

$$\mathbf{F}^0(\mathbf{X}, t) = \frac{1}{V_{\text{RVE}}} \int_{V_{\text{RVE}}} \mathbf{F}(\mathbf{X}, \mathbf{Y}, t, \tau) dV_{\text{RVE}} \equiv \bar{\mathbf{F}} \quad (61)$$

where \mathbf{F}^0 is the macroscopic deformation gradient and $\bar{\mathbf{F}}$ the deformation gradient averaged over the RVE. Velocities can be applied analogously to the boundary nodes as $\mathbf{v}_i = \dot{\mathbf{F}}^0(\mathbf{X}, t) \cdot \mathbf{X}_i$, $\forall i \in \partial V_{\text{RVE}}^D \equiv \partial V_{\text{RVE}}$ in the case of Dirichlet boundary conditions, or only to the corners

$$[\mathbf{v}_1 \quad \mathbf{v}_2 \quad \mathbf{v}_3] = \dot{\mathbf{F}}^0(\mathbf{X}, t) \cdot [\mathbf{X}_1 \quad \mathbf{X}_2 \quad \mathbf{X}_3], \quad (62)$$

with periodicity constraints on the rest of the boundary for periodic boundary conditions. It can also be shown that for these boundary conditions, Dirichlet or periodic,

$$\dot{\mathbf{F}}^0(\mathbf{X}, t) = \frac{1}{V_{\text{RVE}}} \int_{V_{\text{RVE}}} \dot{\mathbf{F}}(\mathbf{X}, \mathbf{Y}, t, \tau) dV_{\text{RVE}} \equiv \dot{\bar{\mathbf{F}}}. \quad (63)$$

If the RVE satisfies relations (61) and (63), it is said to be consistent with the macroscopic variables. $\bar{\mathbf{F}}$ and $\dot{\bar{\mathbf{F}}}$ will be referred to as the macroscopic observables.

5.2 Cauchy-Born rule

If in equation (40), the problem to be solved inside the RVE, the $\mathcal{O}(\epsilon)$ terms are neglected, the particle positions and velocities in the RVE are given as

$$\begin{bmatrix} \mathbf{x}_i \\ \mathbf{v}_i \end{bmatrix} = \begin{bmatrix} \mathbf{F}^0(\mathbf{X}, t) \cdot \mathbf{X}_i \\ \dot{\mathbf{F}}^0(\mathbf{X}, t) \cdot \mathbf{X}_i \end{bmatrix}. \quad (64)$$

This may be a reasonable approximation for small (linear) deformations. It is called the Cauchy-Born hypothesis and is used in many multiscale methods, including the Quasi-Continuum method [21] in regions where a continuum description is considered to be valid. The assumption of a constant deformation gradient over the RVE is also referred to as the Taylor (or Voigt) assumption [25].

The $\mathbf{u}^1(\mathbf{X}, \mathbf{Y}_i, t, \tau)$ terms can be seen as corrections to the Cauchy-Born rule. Correspondingly, the $\mathbf{v}^1(\mathbf{X}, \mathbf{Y}_i, t, \tau)$ terms can be seen as a correction to a linear velocity profile described by the material velocity gradient $\dot{\mathbf{F}}^0(\mathbf{X}, t)$. We now propose two ways of initializing these corrections.

5.3 Elastic equilibrium

First consider the case where the inter-particle forces (and thus the stress) do not depend on the particle velocities, as in [11]. The microscopic problem then reduces to

$$\bar{m}_i \frac{d^2 \mathbf{u}^1(\mathbf{X}, \mathbf{Y}_i, t, \tau)}{dt^2} = \sum_j \bar{\mathbf{f}}_{ij} (\mathbf{F}^0(\mathbf{X}, t) \cdot \mathbf{X}_{ij} + \epsilon [\mathbf{u}^1(\mathbf{X}, \mathbf{Y}_j, t, \tau) - \mathbf{u}^1(\mathbf{X}, \mathbf{Y}_i, t, \tau)]) \quad \forall i \notin \partial V_{\text{RVE}}^D. \quad (65)$$

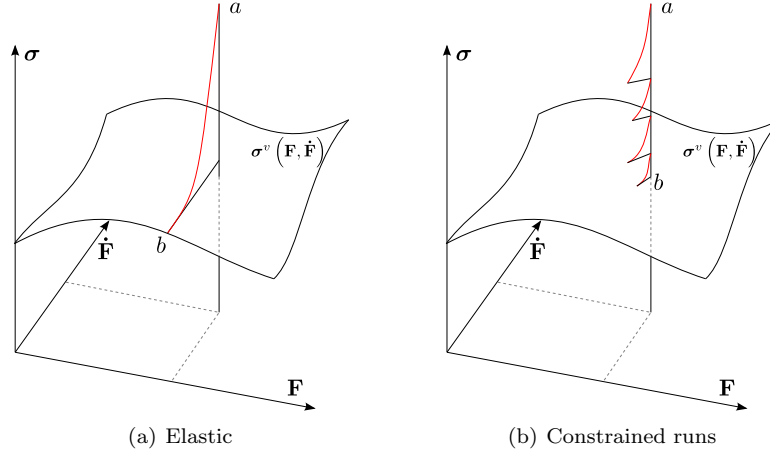


Figure 3: Left: illustration of relaxation to elastic equilibrium. Right: constrained runs initialization, consisting of time-integration (red lines) followed by rescaling.

A possible RVE initialization is the steady-state found by integrating in time until equilibrium, or directly via Newton's method. Integration in time, starting from the Cauchy-Born approximation, relaxes the system of particles and reduces its internal energy, hence minimizing the internal forces and the stress. Using Dirichlet or periodic boundary conditions for the displacements, as described in section 5.1, $\bar{\mathbf{F}}$, the macroscopically observed deformation, stays constant along the red path. In other words, equation (61) is satisfied during the time integration. The particle positions in the elastic equilibrium will be denoted by \mathbf{x}_i^e . Therefore, instead of using (64) for the initialization of the microscopic problem, one can use the improved initialization

$$\begin{bmatrix} \mathbf{x}_i \\ \mathbf{v}_i \end{bmatrix} = \begin{bmatrix} \mathbf{x}_i^e \\ \dot{\mathbf{F}}^0(\mathbf{X}, t) \cdot \mathbf{X}_i \end{bmatrix}, \quad (66)$$

which can be improved further to

$$\begin{bmatrix} \mathbf{x}_i \\ \mathbf{v}_i \end{bmatrix} = \begin{bmatrix} \mathbf{x}_i^e \\ \mathbf{l}^0(\mathbf{X}, t) \cdot \mathbf{x}_i^e \end{bmatrix} \quad (67)$$

where $\mathbf{l} = \partial \mathbf{v}(\mathbf{x}, t) / \partial \mathbf{x} = \nabla \mathbf{v} = \dot{\mathbf{F}} \mathbf{F}^{-1}$ is the velocity field gradient with respect to the deformed coordinates, whereas $\dot{\mathbf{F}}$ is the gradient with respect to the initial configuration. The elastic equilibrium particle positions are thus also used for the determination of the particle velocities. Equation (67) gives a good approximation to the solution of the dynamic microscopic problem (40), provided the inter-particle forces do not depend too strongly on the velocities.

The procedure is illustrated in figure 3(a), where point (a) denotes the first initialization (64), and point (b), which will be called the elastic equilibrium, denotes the steady-state solution of (65). The surface denoted $\sigma^v(\mathbf{F}, \dot{\mathbf{F}})$ in figure 3(a) is a scalar representation of the (viscoelastic) stress, for different macroscopic \mathbf{F} and $\dot{\mathbf{F}}$, as it would be computed from an RVE embedded in a larger microscopic simulation and consistent with that particular \mathbf{F} and $\dot{\mathbf{F}}$.

5.4 Constrained runs iteration

Initialization with the steady state solution of (65) does not use the velocity dependence of the inter-particle forces $\mathbf{f}_{ij}(\mathbf{x}, \mathbf{v})$. Here, an initialization scheme is proposed to initialize both particle positions and velocities at the same time by coupling them through the microscopic dynamics. This scheme consists of two steps: time integration of the RVE, during which the macroscopic observables are allowed to change, followed by a rescaling in order to restore the consistency

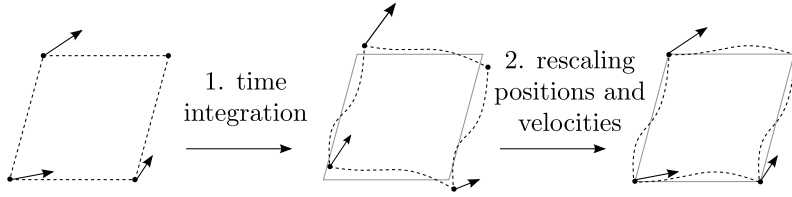


Figure 4: Illustration of the 2 steps of the constrained runs iteration for an RVE deformed with a shear deformation. The arrows at the corners denote the velocities.

with the given macroscopic variables. This is illustrated in figure 3(b). The first step, the time integration, uses periodic boundary conditions, but without keeping the corners fixed. The goal of this step is to bring the state of the RVE closer to the correct microscopic state as would be found in a full microscopic simulation, i.e., the state is attracted to the $\sigma^v(\mathbf{F}, \dot{\mathbf{F}})$ manifold. After the time integration the macroscopic observables, $\bar{\mathbf{F}}$ and $\dot{\bar{\mathbf{F}}}$, have changed and a rescaling is necessary to restore the consistency with the imposed values for the macroscopic observables \mathbf{F}^0 and $\dot{\mathbf{F}}^0$. This rescaling is chosen such that it restores the positions and velocities of the corners according to (60) and (62), while preserving the periodicity of the RVE boundaries, and that it alters the internal configuration of the RVE as little as possible.

Let $\boldsymbol{\mathcal{X}} = [\mathbf{x}_0 \dots \mathbf{x}_n; \mathbf{v}_0 \dots \mathbf{v}_n]$ represent the full state of the RVE, and $\boldsymbol{\mathcal{X}}^0 = [\mathbf{F}^0 \cdot \mathbf{X}_0 \dots \mathbf{F}^0 \cdot \mathbf{X}_n; \dot{\mathbf{F}}^0 \cdot \mathbf{X}_0 \dots \dot{\mathbf{F}}^0 \cdot \mathbf{X}_n]$ the initial guess (64). The time derivative of the state is denoted by

$$\boldsymbol{\mathcal{X}}' = \frac{d\boldsymbol{\mathcal{X}}}{dt} = \begin{bmatrix} \mathbf{v}_0 & \dots & \mathbf{v}_n \\ \mathbf{f}_0(\mathbf{x}_i, \mathbf{v}_i)/m_0 & \dots & \mathbf{f}_n(\mathbf{x}_i, \mathbf{v}_i)/m_n \end{bmatrix}. \quad (68)$$

When using a single forward Euler step, the updated state after integration is

$$\hat{\boldsymbol{\mathcal{X}}}^k = \boldsymbol{\mathcal{X}}^k + \Delta t \boldsymbol{\mathcal{X}}'^k. \quad (69)$$

Then, we first translate the RVE such that corner p_1 is shifted back to the origin. The shifted corners p_2 and p_3 can be mapped to their initial positions by the following linear transformation

$$\mathbf{P}^k \cdot [\hat{\mathbf{x}}_2^k - \hat{\mathbf{x}}_1^k \quad \hat{\mathbf{x}}_3^k - \hat{\mathbf{x}}_1^k] = [\mathbf{F}^0 \cdot \mathbf{X}_2 \quad \mathbf{F}^0 \cdot \mathbf{X}_3]. \quad (70)$$

The combined translation and linear transformation is an affine transformation. Similarly, the velocities can be shifted, so that the velocity of corner p_1 is zero. Then the shifted velocities of corners p_2 and p_3 are transformed with the following affine mapping

$$\mathbf{Q}^k \cdot [\hat{\mathbf{v}}_2^k - \hat{\mathbf{v}}_1^k \quad \hat{\mathbf{v}}_3^k - \hat{\mathbf{v}}_1^k] + [\hat{\mathbf{v}}_2^k - \hat{\mathbf{v}}_1^k \quad \hat{\mathbf{v}}_3^k - \hat{\mathbf{v}}_1^k] = [\dot{\mathbf{F}}^0 \cdot \mathbf{X}_2 \quad \dot{\mathbf{F}}^0 \cdot \mathbf{X}_3]. \quad (71)$$

Note that here the positions are used to interpolate the velocities since the matrix with corner velocities could become singular, which is not the case for the matrix with corner positions. Equations (70) and (71) uniquely define the 2 by 2 matrices \mathbf{P}^k and \mathbf{Q}^k . These rescaling transformations are applied to all particles inside the RVE

$$\boldsymbol{\mathcal{X}}^{k+1} = \begin{bmatrix} \mathbf{P}^k & \mathbf{0} \\ \mathbf{Q}^k & \mathbf{I} \end{bmatrix} \cdot \left(\hat{\boldsymbol{\mathcal{X}}}^k - \begin{bmatrix} \hat{\mathbf{x}}_1^k \dots \hat{\mathbf{x}}_1^k \\ \hat{\mathbf{v}}_1^k \dots \hat{\mathbf{v}}_1^k \end{bmatrix} \right). \quad (72)$$

The time integration (69) followed by the rescaling (72) together form the constrained runs iteration, which is repeated until convergence. In the next section, the three strategies to reconstruct the microscopic state inside the RVE are compared for a numerical example.

6 Numerical results

As a numerical example, we use the microscopic model for plant parenchyma tissue described previously, with the parameters also taken from [27]. A plant cell measures $25 \times 25 \mu\text{m}$ where each

25 μm side of the cell wall is discretized using 11 discrete elements and the cells are filled with 16 SPH particles. The fluid density $\rho = 1000 \text{ kg/m}^3$ and the SPH particle mass $m_i^{\text{SPH}} = 2.7 \cdot 10^{-12} \text{ kg}$ correspond to that of water, while its viscosity was set to $\mu = 10^{-2} \text{ Pa} \cdot \text{s}$. To convert the density and viscosity to two-dimensional quantities, we assume a constant thickness of the plant tissue of $10 \mu\text{m}$. The SPH smoothing length is set to $5.5 \mu\text{m}$ and the speed of sound to $c_s = 50 \mu\text{m/s}$. The mass of a cell wall particle is $m_i^{\text{DEM}} = 0.5 \cdot 10^{-12} \text{ kg}$ and the cell wall elastic modulus is set to $k_w = 4000 \text{ N/m}$. In [27], the viscous damping constant γ_c was set to a minimum, to approximate a purely elastic wall while ensuring stability of the simulation, but mainly because of lack of experimental data. Here, we have chosen to critically damp the cell wall. The repulsive force strength is set to $\lambda = 5 \cdot 10^5$ and the cutoff distance to $x_0 = 10 \mu\text{m}$. The system of DEM and SPH particles is integrated in time with a leapfrog integrator with fixed time step $\delta t = 10^{-4} \mu\text{s}$.

First we look in detail at the different initialization procedures applied to a single RVE consisting of a single plant cell. Cauchy-Born approximation, elastic equilibrium and constrained runs will respectively refer to (64), (67) and (69)-(72). Then a full microscopic simulation for a large domain is compared to the coupled multiscale simulation.

6.1 Initialization comparison

To demonstrate the different RVE initializations we take a single plant cell as an RVE, using periodic boundary conditions. Starting from this cell in its equilibrium state, a shear deformation is applied in 20 steps according to

$$\mathbf{F}_\alpha = \begin{bmatrix} 1 & 0.01\alpha \\ 0 & 1 \end{bmatrix} \quad \text{for } \alpha = 0, 1, \dots, 20. \quad (73)$$

First, in each step the average velocity of the RVE is assumed to be zero, $\dot{\mathbf{F}} = \mathbf{0}$. To initialize the state of the RVE due to $\mathbf{F}_{\alpha+1}$ we first apply the incremental deformation gradient $\Delta\mathbf{F} = \mathbf{F}_{\alpha+1}(\mathbf{F}_\alpha)^{-1}$ to the RVE as deformed by the previous deformation gradient \mathbf{F}_α . This corresponds to the Cauchy-Born approximation. For the initialization using elastic relaxation and constrained runs iteration, further internal RVE relaxation is performed according to (67) and (69)-(72). Figure 5(left) shows the σ_{xy} (top) and σ_{xx} (bottom) components of the average stress over the RVE, after each of these three initializations. As expected, elastic relaxation and constrained runs reduce the stress (in absolute value) as compared to the Cauchy-Born approximation. Since the velocity gradient is zero, the constrained runs iteration converges to the elastic equilibrium. Figure 5(right) shows the same but with a velocity gradient

$$\dot{\mathbf{F}} = \begin{bmatrix} 0 & 0.01 \\ 0 & 0 \end{bmatrix}, \quad (74)$$

applied to the RVE in each step. Recalling the expression for the SPH inter-particle forces (8), we recognize a static pressure term, and a velocity dependent viscosity term. The constrained runs iteration finds the particle positions as a trade-off between pressure and viscosity forces while the elastic relaxation only considers the pressure forces; viscosity forces are zero in elastic equilibrium. This intuitively explains why the σ_{xx} component of the stresses computed by constrained runs and elastic relaxation do not coincide. The fourth line, labeled ‘‘full microscopic time integration’’ in figure 5(right) is computed by moving the corners of the RVE with a fixed velocity according to $\dot{\mathbf{F}}$, applying periodic boundary conditions and integrating continuously in time, starting from the RVE equilibrium state. After an initial relaxation, the stress in the RVE comes relatively close to that computed after constrained runs initialization, see figure 5(bottom-right).

A more in-depth look at an initialization with \mathbf{F}_{10} and $\dot{\mathbf{F}}$ from (74) starting from an undeformed RVE is presented in figure 6. Let the error between two RVE states be defined as the 2-norm of the difference of their state matrices \mathcal{X} , as defined in 5.4. Figure 6(left) shows this error from the reference solution as computed by full microscopic integration for initialization using elastic relaxation and constrained runs iteration as a function of the number of relaxation steps or constrained runs iterations. As could also be concluded from figure 5, the initialization using

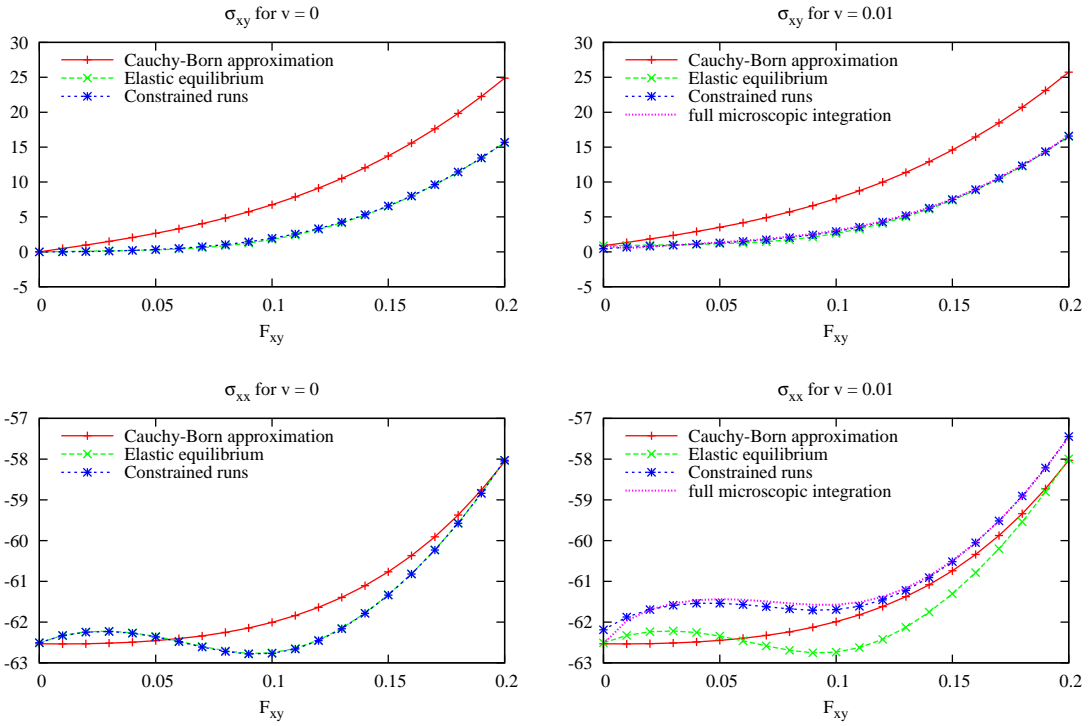


Figure 5: The σ_{xy} (top) and σ_{xx} (bottom) components of the stress tensor in an RVE deformed by \mathbf{F}_α (73). Left: average velocity gradient $\dot{\mathbf{F}} = \mathbf{0}$: the elastic relaxation and constrained runs solutions coincide. Right: velocity gradient with $\dot{F}_{xy} = 0.01$ (v on the figure). The line labeled 'full microscopic integration' was obtained by continuously integrating in time an RVE which is shear deformed with constant velocity.

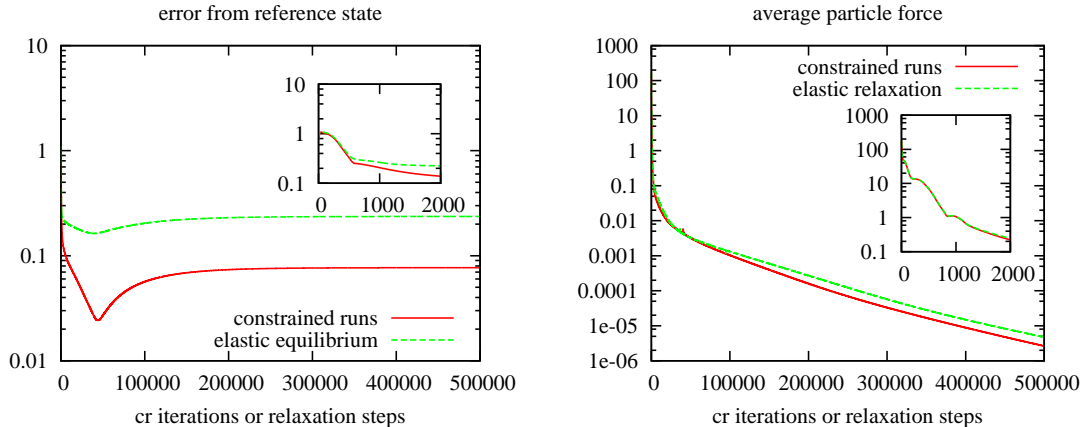


Figure 6: Left: error w.r.t. the reference state for the initialization by a) elastic relaxation and b) constrained runs as a function of relaxation steps or constrained runs (cr) iterations. Right: average particle force as a function of relaxation steps or constrained runs (cr) iterations. The average force, and thus the particle accelerations go to zero.

constrained runs more accurately reconstructs the microscopic state. Figure 6(right) shows the average force off all particles in the RVE as a function of the number of relaxation steps or constrained runs iterations. As expected for the elastic relaxation, the total particle forces and thus also the particle accelerations, go to zero as the RVE converges to the steady state. However, the accelerations will no longer be zero when the velocity gradient is applied to the elastic equilibrium of the RVE. From figure 6(right) we conclude that the constrained runs iteration also converges to a state with zero accelerations for all particles. We can thus use this measure for the average particle force in a stopping criterion for both the elastic relaxation and the constrained runs iteration, see 6.2. During the first few thousand steps, the average particle force decreases rapidly, while after that it slowly goes to machine precision. For smaller incremental deformations, only a few hundred steps are needed to significantly reduce the average particle force, see also 6.2.

6.2 Bending bar

As a test scenario, a square piece of plant tissue fixed on the left side and bending under the influence of a body force of $0.2 \mu\text{m}/(\mu\text{s})^2$ pointing downward is considered. The domain, $400 \times 400 \mu\text{m}$, consists of 16×16 individual square plant cells, stacked in a regular grid, see figure 7(left). The same square domain is also discretized using 4×4 bilinear quadrilateral finite elements, see figure 7(right). The deviatoric part of the stress tensor $\boldsymbol{\sigma} - \text{tr}(\boldsymbol{\sigma})/2$ is integrated with a standard 2×2 point Gauss quadrature rule, while the hydrostatic pressure $\text{tr}(\boldsymbol{\sigma})/2$ is under-integrated with a one point Gauss quadrature rule. This approach, called selective reduced integration, improves the elements convergence by reducing volumetric locking [18]. The finite element system (58) is integrated in time using the explicit Runge-Kutta code Dopri [12] with an absolute error tolerance 10^{-5} and a relative tolerance 10^{-3} . The mass matrix is constant and is thus factorized only once. The macroscopic density is computed by dividing the sum of all particle masses in the microscopic simulation by the total domain area.

Since the microscopic structure is periodic, one period, i.e. one plant cell, is taken as the RVE. The deformation and velocity gradient at each quadrature point are given as input to an RVE centered around the quadrature point. After initialization of the RVE, the stress tensor is computed using (57b). Figure 8 shows the vertical displacement of a point in the middle of the right boundary of the domain as a function of time for the three different RVE initialization strategies. Relaxation of the RVE to its elastic equilibrium is also done using the leapfrog integrator with

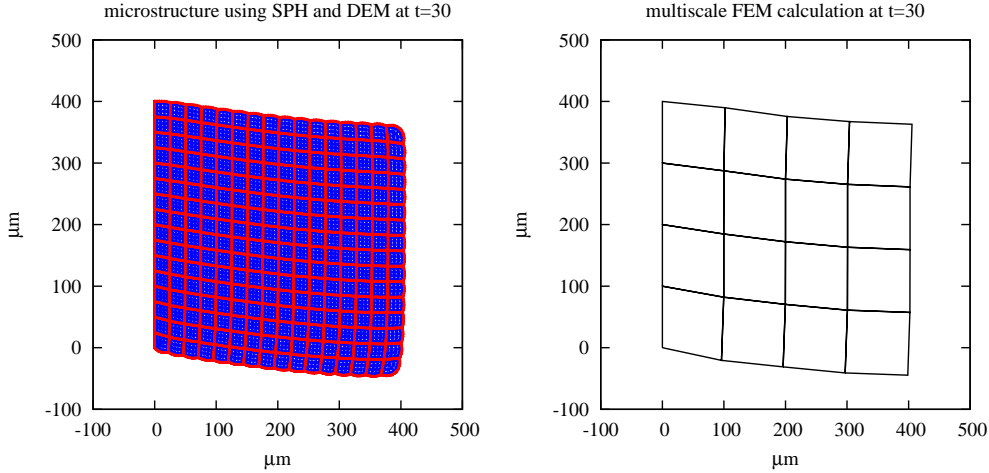


Figure 7: Left: full micro 16×16 cells. Here the SPH particles are in blue, the cell wall particles in red. Right: coupled multiscale computation. Each finite element uses $4+1$ quadrature points, so in total $4 \times 4 \times 5$ RVEs, one cell each, are kept in memory.

$\delta t = 10^{-4} \mu s$. The time integration step in the constrained runs iteration uses a single forward Euler step with $\delta t = 10^{-4} \mu s$. Relaxation to the elastic equilibrium and the constrained runs iteration are stopped when the average particle force becomes less than 1.0. Experiments with a lower bound for the average force did not significantly improve the results. On average 230 constrained runs iterations were needed to relax the average particle force below 1.0. The macroscopic time integrator used 4976 function evaluations for 829 computed time steps. The number of function evaluations in the macroscopic time integrator times the average number of constrained runs iterations, $4976 \times 230 = 1144480$, should be compared to the total number of microscopic time steps in the full microscopic integration, which is 2500000. The speedup in time is thus roughly a factor 2.1.

Figure 8 shows the differences between the three initialization procedures. The Cauchy-Born approximation does not relax the RVE and thus severely underestimates the macroscopic displacements. Since the stresses are overestimated, the material seems stiffer than it actually is. Relaxation to elastic equilibrium, with a linear velocity profile applied afterward, see equation (67), correctly computes the elastic part of the stress (oscillation around correct steady state), but introduces artificial damping. Initialization with the constrained runs iteration successfully reduces this artificial damping.

6.3 Discussion

The micro/macro numerical computation is subject to numerical errors of different types, which will fall into the following three categories: microscopic discretization errors, macroscopic discretization errors, multiscale coupling errors. Note that most errors behave similar as in the purely elastic case, see also [11] for a more detailed analysis.

In this work, we do not elaborate on the micro discretization errors (for instance SPH interpolation errors), since they affect both the full microscopic simulation and the coupled multiscale method. However, caution is necessary since the SPH momentum equation (8) does not exactly conserve angular momentum and thus results in a slightly asymmetric Cauchy stress tensor. In the finite element computations the asymmetric stress tensor was used since it led to better results than using only the symmetric part of the Cauchy stress tensor. We note that alternative expressions for the momentum equation that better conserve angular momentum are to be preferred.

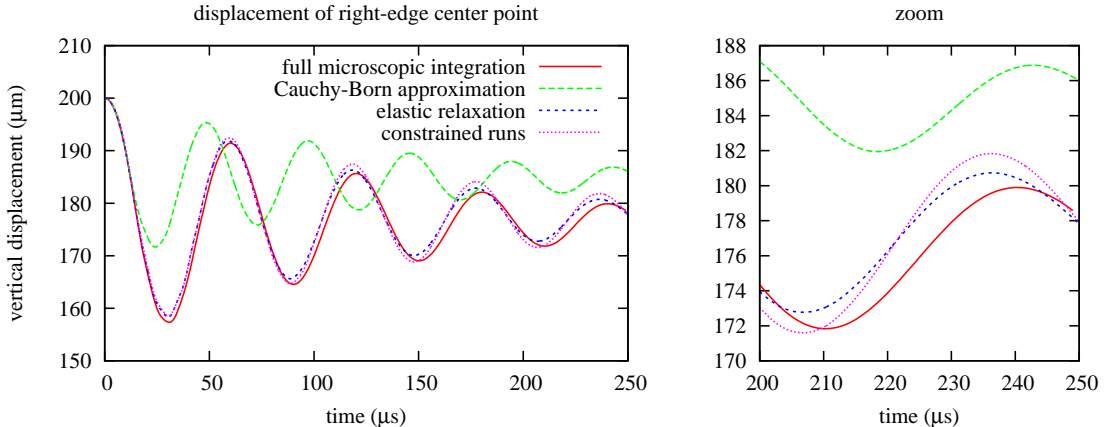


Figure 8: The macroscopic evolution, represented by its vertical displacement, of a point in the middle of the right side of the domain is plotted as function of time. Computation using the full microscopic model is compared to the coupled multiscale method for three different RVE initialization approaches.

Decreasing the finite element mesh size increases the accuracy, but the mesh should not be refined beyond the microscopic resolution, see [11]. Likewise, the accuracy of the time integration at macro level should not exceed the accuracy of the stress tensor, i.e., the tolerances used in the stopping criterion for constrained runs and the elastic relaxation.

As the multiscale method relies on the separation in spatial scales, the typical microscopic length scale, the RVE size, should be small compared to the typical macroscopic length scale, the finite element mesh size. The remaining difference between full micro and multiscale using constrained runs initialization in figure 8 is mainly due to this finite size effect. For larger domains, the size of the RVE will relatively become smaller, yielding a larger separation in spatial scales and relatively more accurate results, see [11].

In the finite element computations the main cost is in the microscopic simulation, the reconstruction of the microscopic state inside the RVE. The Cauchy-Born approximation of the microscopic state does not require any relaxation steps and is thus very fast but quite inaccurate. Elastic relaxation and constrained runs iteration on the other hand are time consuming but lead to more accurate reconstruction of the microscopic RVE state. The accuracy of the initialization can be controlled by the stopping criterion of the relaxation or constrained runs iteration. This allows to control the trade-off between computational efficiency and accuracy. The challenge is to find a stopping criterion that breaks the iteration as soon as the accuracy of the full microscopic simulation is reached.

In the coupled multiscale computations only a fraction of the number of cells is simulated compared to the full microscopic run. For larger domains the number of plant cells has to increase, while the number of finite elements only depends on the desired accuracy, not on the domain size. Thus a larger separation in spatial scales leads to larger computational benefit for the multiscale method. Furthermore, the multiscale method can also benefit from a possible separation in temporal scales. Several restrictions, including the CFL condition, enforce the use of a small time step δt throughout the microscopic simulation. On the macroscopic scale, the material behaves much smoother, allowing a time step of several orders of magnitude larger. Evolving the microscopic model over a macroscopic time interval ΔT could be done using microscopic time integration with m microscopic time steps such that $m \delta t = \Delta T$ or by applying the incremental deformation gradient followed by one of the initialization procedures. A speedup is achieved when the number of iterations in the relaxation is less than m .

7 Conclusions and outlook

The multiscale approach described in this work is an extension of the RVE based hierarchical multiscale technique as described in [15, 11] to also deal with the velocity dependence of the stress tensor. This dependence of the Cauchy stress on the velocity followed automatically from the velocity dependence of the inter-particle forces in the microscopic model, i.e. a model consisting of both smoothed particle hydrodynamics and discrete elements. The macroscopic model and the stress expression were derived from the microscopic model using generalized mathematical homogenization, as originally proposed by Chen and Fish [5, 4, 8]. The method as presented here applies to viscoelastic fading memory materials and may yield a considerable computational gain. An example of such viscoelastic material behavior was given by a model for plant parenchyma tissue.

Since here also velocity is considered as macroscopic observable, the RVE should be initialized not only with the macroscopic deformation gradient but also with the current macroscopic velocity gradient, which complicates the RVE initialization procedure considerably. We consider three possible initializations. The first initialization, based on the Cauchy-Born rule, leads in our context to inaccurate results, from which we conclude that internal relaxation of the RVE is necessary. Two relaxation strategies are described. The first, a simple relaxation to elastic equilibrium followed by applying the velocity gradient to the steady state of the RVE still introduced some artificial damping (viscosity) at the macroscopic scale. We therefore proposed a scheme, called the constrained runs iteration, to initialize both particle positions and velocities at the same time. This approach explicitly uses the inter-particle dependence on the velocities and succeeds in reducing the artificial damping.

In a numerical example, a multiscale simulation of the time dependent deformation of plant parenchyma cells, the importance of a good initialization was demonstrated. It was shown that the constrained runs initialization succeeds in reducing both artificial stiffness and artificial damping. However, a detailed analysis of convergence and stability properties of this initialization procedure are left as a subject for future research.

Acknowledgments

The finite element code was developed using the deal.II C++ library [1]. This paper presents research results of the Belgian Network DYSCO (Dynamical Systems, Control, and Optimization), funded by the Interuniversity Attraction Poles Programme, initiated by the Belgian State, Science Policy Office. The scientific responsibility rests with its authors. This research was supported by the Fund for Scientific Research – Flanders through Research Project (3E060094). GS is a Post-doctoral Fellow of the Research Foundation - Flanders (FWO). The simulations were performed on the computer cluster of the HPC Computing Initiative, funded by the Katholieke Universiteit Leuven Research Council.

References

- [1] W. Bangerth, R. Hartmann, and G. Kanschat. deal.II — a general-purpose object-oriented finite element library. *ACM Transactions on Mathematical Software*, 33(4):24, August 2007. Article 24, 27 pages.
- [2] J. Bonet and R. D. Wood. *Nonlinear continuum mechanics for finite element analysis*. Cambridge University Press, 1997.
- [3] D. M. Bruce. Mathematical modelling of the cellular mechanics of plants. *Philosophical Transactions of the Royal Society B: Biological Sciences*, 358:1437–1444, 2003.

- [4] W. Chen and J. Fish. A generalized space-time mathematical homogenization theory for bridging atomistic and continuum scales. *International Journal for Numerical Methods in Engineering*, 67(2), 2006.
- [5] W. Chen and J. Fish. A mathematical homogenization perspective of virial stress. *International Journal for Numerical Methods in Engineering*, 67:189–207, 2006.
- [6] P. A. Cundall and O. D. L. Strack. A discrete numerical model for granular assemblies. *Geotechnique*, 29(1):47–65, 1979.
- [7] F. Feyel and J. L. Chaboche. FE2 multiscale approach for modelling the elastoviscoplastic behaviour of long fibre SiC/Ti composite materials. *Computer Methods in Applied Mechanics and Engineering*, 183(3):309–330, 2000.
- [8] J. Fish, W. Chen, and R. Li. Generalized mathematical homogenization of atomistic media at finite temperatures in three dimensions. *Computer Methods in Applied Mechanics and Engineering*, 196(4-6):908 – 922, 2007.
- [9] C. W. Gear, T. J. Kaper, I. G. Kevrekidis, and A. Zagaris. Projecting to a Slow Manifold: Singularly Perturbed Systems and Legacy Codes. *SIAM Journal on Applied Dynamical Systems*, 4:711, 2005.
- [10] C. W. Gear and I. G. Kevrekidis. Constraint-defined manifolds: a legacy code approach to low-dimensional computation. *Journal of Scientific Computing*, 25(1):17–28, 2005.
- [11] P. Ghysels, G. Samaey, B. Tjjskens, P. Van Liedekerke, H. Ramon, and D. Roose. Multi-scale simulation of plant tissue deformation using a model for individual cell mechanics. *Phys. Biol*, 6(016009):016009, 2009.
- [12] E. Hairer, S. P. Nørsett, and G. Wanner. *Solving ordinary differential equations I: nonstiff problems*. Springer, 1993.
- [13] I. G. Kevrekidis, C. W. Gear, J. M. Hyman, P. G. Kevrekidis, O. Runborg, and C. Theodoropoulos. Equation-free, coarse-grained multiscale computation: Enabling microscopic simulators to perform system-level analysis. *Communications in Mathematical Sciences*, 1(4):715–762, 2003.
- [14] I. G. Kevrekidis and G. Samaey. Equation-free multiscale computation: algorithms and applications. *Annual Review of Physical Chemistry*, 60:321–344, 2009.
- [15] V. Kouznetsova, W. A. M. Brekelmans, and F. P. T. Baaijens. An approach to micro-macro modeling of heterogeneous materials. *Computational Mechanics*, 27:37–48, 2001.
- [16] M. B. Liu. *Smoothed particle hydrodynamics: a meshfree particle method*. World Scientific Pub Co Inc, 2003.
- [17] R. Lu and V. M. Puri. Characterization of nonlinear creep behavior of two food products. *Journal of Rheology*, 35:1209, 1991.
- [18] D. S. Malkus and T. J. R. Hughes. Mixed finite element methods- Reduced and selective integration techniques- A unification of concepts. *Computer Methods in Applied Mechanics and Engineering*, 15:63–81, 1978.
- [19] T. J. Massart, R. H. J. Peerlings, and M. G. D. Geers. An enhanced multi-scale approach for masonry wall computations with localization of damage. *International journal for numerical methods in engineering*, 69(5):1022–1059, 2007.
- [20] C. Miehe, J. Schroder, and J. Schotte. Computational homogenization analysis in finite plasticity simulation of texture development in polycrystalline materials. *Computer Methods in Applied Mechanics and Engineering*, 171(3-4):387–418, April 1999.

- [21] R. E. Miller and E. B. Tadmor. The quasicontinuum method: Overview, applications and current directions. *Journal of Computer-Aided Materials Design*, 9:203–239, October 2002.
- [22] J. P. Mittal, N. N. Mohsenin, and M. G. Sharma. Rheological characterization of apple cortex. *Journal of Texture Studies*, 18(1):65–93, 1987.
- [23] J. J. Monaghan. Smoothed particle hydrodynamics. *Annual review of astronomy and astrophysics*, 30(1):543–574, 1992.
- [24] J. P. Morris, P. J. Fox, and Y. Zhu. Modeling low Reynolds number incompressible flows using SPH. *Journal of Computational Physics*, 136(1):214–226, 1997.
- [25] G. I. Taylor. Plastic strain in metals. *J. Inst. Metals*, 62(1):307–324, 1938.
- [26] P. Van Liedekerke, E. Tijskens, P. Ghysels, G. Samaey, D. Roose, and H. Ramon. A particle based model to simulate the micromechanics of single plant cells and aggregates. *Submitted*, 2009.
- [27] P. Van Liedekerke, E. Tijskens, H. Ramon, P. Ghysels, G. Samaey, and D. Roose. A particle based model to simulate plant cells dynamics. In *Proceedings of the 4th international SPHERIC workshop, Nantes, France*, 2009.
- [28] O. C. Zienkiewicz and R. L. Taylor. *The Finite Element Method for Solid and Structural Mechanics, Sixth Edition*. Butterworth-Heinemann, 2005.